LAWRENCE
LIVERMORE
NATIONAL
LABORATORY

LLNL-JRNL-823504

Characterization of thermal transport and evolution of Au plasma in ICF experiments by Thomson scattering

G. F. Swadling, C. Bruulsema, W. A. Farmer, M. Sherlock, M. D. Rosen, J. S. Ross, W. Rozmus

June 14, 2021

Physics of Plasmas

Disclaimer

Characterization of thermal transport and evolution of Au plasma in ICF experiments by Thomson scattering

C. Bruulsema,[1,2] W. A. Farmer,[3] M. Sherlock,[3]
G. F. Swadling,[3] M. D. Rosen,[3] J. S. Ross,[3] and W. Rozmus[1]

[1]*Theoretical Physics Institute, Department of Physics, University of Alberta, Edmonton, Alberta, T6G 2E1, Canada*

[2]*Corresponding author, bruulsem@ualberta.ca*

[3]*Lawrence Livermore National Laboratory, 7000 East Ave., Livermore, CA 94550, USA*

Abstract

The paper demonstrates the capability of optical Thomson scattering (OTS) to measure thermal transport, and provides support to radiation hydrodynamic and kinetic simulations of electron thermal transport and plasma evolution. OTS theory and plasma simulations are applied to the interpretation of experimental measurements of laser-produced plasma from spherical gold targets on the OMEGA laser facility. The dynamical form factor, $S(\vec{k},\omega)$, of electron density fluctuations that is used in the fitting of Thomson scattering spectra includes ion-ion collisions and effects of non-Maxwellian distribution functions. OTS measurements and their interpretation are consistent with the nonlocal transport model in radiation hydrodynamic simulations as well as with kinetic simulations in the second half of the probe pulse duration. In particular, the reversal of heat transport during cooling is observed to be consistent with simulations, while some discrepancies are noted during the initial heating of the Au targets.

LLNL-JRNL-823504

I. INTRODUCTION

In this paper we present a study of heat transport in a laser-ablated Au plasma. Electron heat flux in Inertial Confinement Fusion (ICF) plasmas is a kinetic process, and remains an outstanding problem, and is the subject of active and intense research within the ICF field [1]. The overarching aim of this work is to improve our understanding of thermal transport under ICF hohlraum-relevant plasma conditions, in order to facilitate the development of predictive models that can be used to design new and better hohlraums without the need for the significant experimental testing currently required to validate new designs. The main result of this work is that we are able to show that while simulations can accurately match the measured heat flow at late times, they significantly over-predict thermal transport in the early phases of the experiment. This observation is in agreement with previously developed, macroscopic models of hohlraum plasma evolution have also found the need to artificially lower heat flux early on in laser shots [2, 3]. In this paper we show that the discrepancy between the experimental measurement and simulation can be explained by a combination of a strong super-Gaussian distortion of the electron distribution function which is not fully modeled in simulations, combined with the presence of steep density gradients in the expanding plasma at early time.

The plasmas studied in this paper are produced in directly-driven experiments conducted at the OMEGA laser facility at the Laboratory for Laser Energetics, University of Rochester. Targets are gold and beryllium coated spherical bead targets [4, 5]. Electron heat flux can be quantified using measurements of the temperature and density gradients and the particle distribution functions [6–10]. In this work we use a combination of collective optical Thomson scattering (OTS) measurements, radiation-hydrodynamic simulations of the plasma dynamics and Vlasov-Fokker-Planck (VFP) simulations of the particle kinetics to characterize the particle distribution functions within the measured scattering volume and extract heat flux measurements.

The OMEGA Thomson scattering system is used to obtain scattering spectra from ion-acoustic wave (IAW) and electron plasma wave (EPW) fluctuations in the ablated plasma. These spectra are analyzed to obtain the time evolution of electron temperature and plasma density at the measurement location. OTS is a powerful diagnostic technique that can provide uniquely local measurements of plasma parameters in high energy density plasmas. This technique has been applied extensively to make comprehensive studies of the plasma parameters [4, 11], distribution functions [12–14], magnetic fields and electric currents [15, 16] and thermal transport [6, 17–19] in a variety of laser

driven plasmas, with particular emphasis on ICF hohlraum plasmas [20]. To infer the basic plasma parameters from the OTS spectra, one relies primarily on the spectral displacements of the resonant peaks in the collective regime of the OTS. Good accuracy is usually achieved in such a procedure without invoking the effects of non-Maxwellian distribution functions and particle collisions in the theory of the dynamical form factor (2). Large scale radiation hydrodynamic simulations, which include the effects of non-local thermal transport, are used to calculate the expected evolution of the electron temperature and plasma density gradients for the analysis of the particle transport. These simulations have been benchmarked against Thomson scattering measurements and shown to successfully reproduced the evolution of the electron temperature and plasma density [4, 5].

Heat flow is measured in our experiments through a more careful analysis of optical Thomson scattering (OTS) data; this analysis forms the main focus of this paper. Broadly, diagnosis of the heat flow is achieved via an analysis of its effect on the relative intensity of two ion-acoustic scattering peaks. The scattering spectrum can only be sensitive to this effect when the scattering geometry is selected such that the wave vectors of the observed density fluctuations point along the direction of the heat flow, i.e. the radial expansion vector of the plasma for the sphere experiments (Fig. 1). Electron heat flow is dominated by the tail of the electrons distribution, at velocities much greater than the ion acoustic velocity of the plasmas. This flow of electrons in the tail induces an electric field which drives a return current, shifting the bulk of the electron distribution function slightly with respect to the ion flow velocity. The result of this shift is that the gradient of the electron distribution function at the phase velocities of the two counterpointing ion acoustic waves can be different, leading to a difference in the Landau damping rates and therefore the amplitude of the two peaks. We are therefore able to measure heat flow indirectly through our more direct measurements of this return current. Analysis of this effect proceeds by accounting first for the instrumental effects in the OTS measurements such as angular spreads of the probe and collection optics, which are particularly important in flowing plasmas, as well as frequency broadening due to pulse front tilt [21]. The theory of the dynamical factor, $S(\vec{k},\omega)$ must be expanded beyond the collisionless model that is typically used, and include the effect of ion-ion (i-i) collisions in the highly ionized Au plasmas [22, 23]. Damping of the IAWs due to i-i collisions is small and comparable with the electron Landau damping and its effect on spectral broadening is negligible as compared with the instrumental width of IAW peaks in the OTS spectrum. However, in the analysis of the relative intensity of IAW peaks due to the drift velocity of the electrons, we find that the i-i collision effects are important and cannot be neglected when analysing the relative amplitudes of

the IAW. We must also account for the effects of the non-equilibrium electron distribution functions (EDF). The electron density correlation function and the dynamical form factor are sensitive to the form of the EDF, as the damping rate of each ion acoustic peak is sensitive to the gradient of the EDF at its phase velocity. The non-equilibrium EDFs that are produced by the inverse bremsstrahlung (IB) heating [24] or thermal transport [7] can be measured experimentally through the EPW feature of the OTS spectrum [14] [25] and applied to the calculations of plasma parameters and the heat flux.

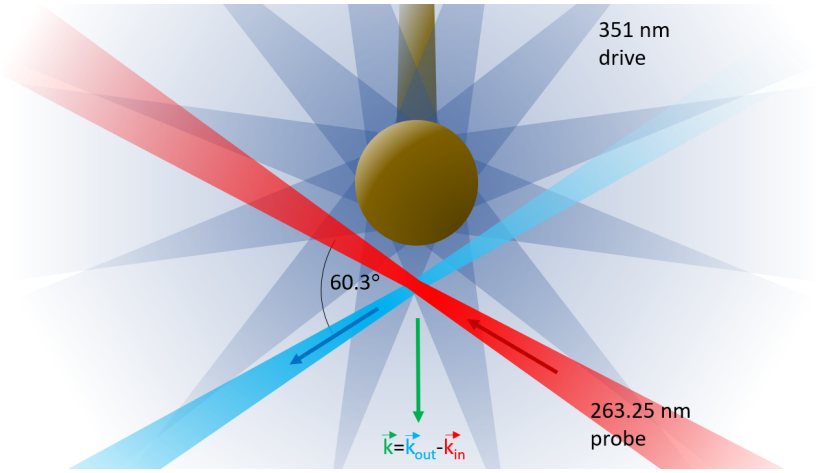

FIG. 1: Thomsons Scattering probe and collection geometry, observing plasma at 730 μm from the sphere center. The probe beam is shown in red, with the collection volume in light blue and the resulting wave vector probed in green.

Using these measurements of the electron return current, we have found that at late times (t > 1ns) the inferred heat flux is consistent with the nonlocal Schurtz-Nicolai-Busquet (SNB) [26] model and VFP simulations [7]. The spatial profiles of plasma density and electron temperature predicted by the radiation hydrodynamic simulations employing the SNB model disagree with the Spitzer-Härm local transport theory predictions. The OTS measurements also display the change in the direction of the heat flux in response to rapid radiation cooling of the dense plasma near the target surface after the termination of the heating beams. However, a disagreement between measurements of the heat flux and simulation results is seen early in the plasma evolution, $t \leq 1$ ns.

We propose that this discrepancy is the result of the combination of two effects, the super-Gaussian form of the symmetric part of the EDF due to IB heating and the presence of steep density gradients at early time [8, 27]. While for most of the simulation and laser pulse duration, modest changes in the exponent of the EDF have a small effect on the transport calculations, at early times the relatively stronger density gradient can reduce the electron heat flux. This is a consequence of the transport relations for the heat flux in non-equilibrium plasmas with super-Gaussian EDFs, which include terms proportional to the density gradients that have negative contributions as compared to the terms proportional to the temperature gradient [8], leading to an observable suppression of thermal transport. This feature of the local transport theory is seen in VFP simulations containing nonlocal effects.

The paper is organized as follows: Section II A first introduces the details of the Thomson Scattering measurement taken, and then Section II B summarizes the main results of the radiation hydrodynamic simulations and comparison with the basic interpretation of the OTS measurements. Section III outline models and simulations of heat flux. The main results of the paper for the electron heat flux calculations are shown in Sec. IV. Section V discusses the implications of this work and gives summary of our results.

II. RADIATION HYDRODYNAMIC SIMULATIONS AND COMPARISON WITH THE BASIC OTS RESULTS

Experimental measurements and radiation-hydrodynamic simulations that are relevant to the current study were described in the recent paper Ref. [5] and form part of an ongoing campaign of experiments on the Omega laser facility that use directly illuminated Be and Au spherical targets [4] to investigate laser coupling, heat transport and radiation conversion efficiency in order to improve our understanding of ICF hohlraum physics.

To summarize, the target is a 0.86 mm diameter gold coated bead. Its surface is heated using 59 of the OMEGA heater beams; one beam is used to generate the OTS probe. Phase plates are used to shape the beam intensity at the target to produce a reasonably smooth intensity distribution over the target surface of $5 \times 10^{14} W/cm^2$ for 2 ns, delivering $21.9 kJ$. The surface of the sphere is ablated and expands rapidly outwards as a hot plasma, which is measured with a Thomson probe at 730 μm from the target center.

We will compare transport in the radiation hydrodynamics simulation with detailed calculations

of the observed electron heat flux from the OTS spectra. We begin with the summary of the OTS measurements and their basic interpretations and by recalling radiation-hydrodynamic simulation results.

A. OTS in Au plasmas

The optical Thomson scattering spectra are recorded with a scattering vector in the radial direction, making the spectra sensitive to components of the flow and density fluctuation propagation velocities in the radial velocity distribution.

The EPW image typically includes significant self emission from the hot plasma in addition to the Langmuir wave fluctuations. This background must be removed to fit the EPW. To do this, radiation from light in the collection cone is subtracted by measuring light outside of the region of the streak camera where the EPW signal is expected (red lines, Fig. 2a). Between the horizontal lines, the time dependence of the of the background radiation is measured, and the region between the vertical lines is used to measure the wavelength dependence. These are assumed to be independent, and multiplied to produce a background radiation image which can be subtracted from the raw signal to produce the EPW data, shown in Fig. 2b.

Because this background subtraction method is imperfect, electron temperature is measured through the separation of the two IAW peaks, using the simulated ionization level of Z=50 (shown in Fig. 2c). Density can subsequently be measured by the shift seen in the cleaned EPW image, shown in Fig. 2b. This is more robust than EPW electron temperature measurements when significant background may still be present with feature scales similar to the width of the EPW, as the shape of the Langmuir waves may be distorted.

To properly and accurately fit the TS spectra, a range of important effects on the spectral shape must be taken into account, based on the details of the measurement geometry and the plasma conditions.

OTS spectra (seen in Fig. 2) were taken in the corona at approximately 735 μm from the sphere center, (305 μm from the surface) 20° from the pole opposite to the stalk. The probe is pointed at 730 μm, but 5 μm of outwards refraction is expected. The probe is focused at f/6.7, with a wavelength of 263.25 nm. The pulse shape is similar to that of the 2 ns drive, but delayed by roughly 0.4 ns. The probe energy was 96.5J with a radius of 35 μm.

Light scattered from the probe is collected with a reflective telescope of focal length of f/10

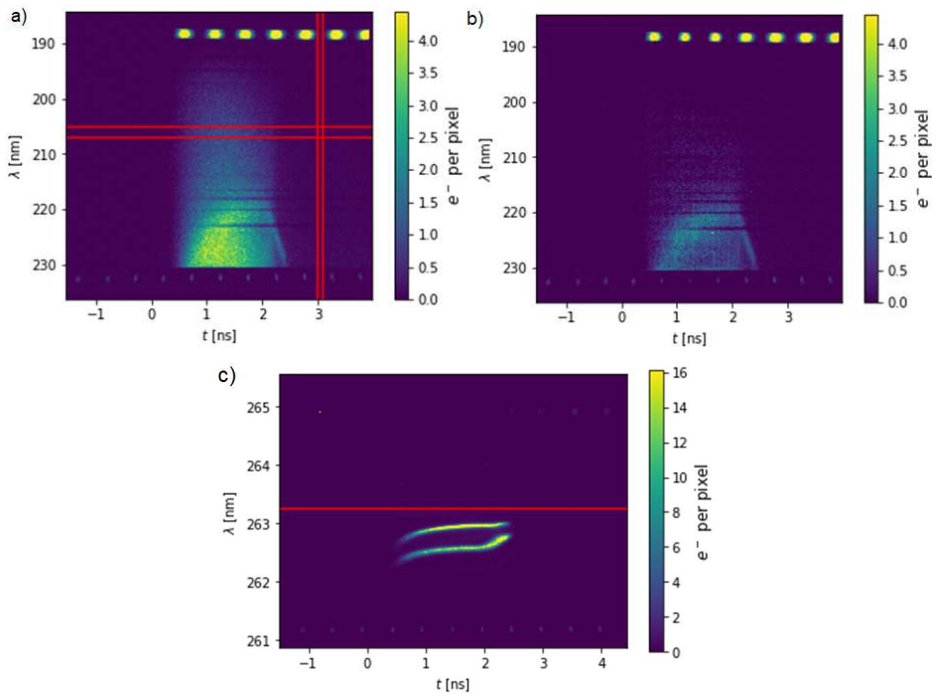

FIG. 2: Thomson scattering images taken in the radial scattering direction, available at ref. [28]. a) Raw EPW spectrum, with red lines marking where profiles are taken for background subtraction. b) EPW spectrum after background subtraction. c) Raw IAW spectrum, with red line denoting the probe wavelength. [Associated dataset available at https://doi.org/10.5281/zenodo.4950679] (Ref. [28]).

at 60.3°, and deposited through separate Czerny-Turner optical spectrometers onto ROSS optical streak cameras [29]. The wave vector observed in this scattering process is $\vec{k} = \vec{k_{out}} - \vec{k_{in}}$, where $\vec{k_{out}}$ is the wave vector of the scattered light and $\vec{k_{in}}$ is the wave vector of the probe. $\vec{k}$ is oriented along the target normal, making the scattered light sensitive to the expansion flow velocity of the plasma.

The electromagnetic waves scattered in the plasma follow the dispersion relation $\omega^2 = \omega_{pe}^2 + k^2c^2$, where ω_{pe} is the plasma frequency in the OTS volume. The light at a scattered frequency is sensitive to the particles and waves traveling at phase velocity $v_{phase} = (\frac{\omega_{out}-\omega_{in}}{k_{out}})\hat{k}$. For this reason

the IAW spectrometer is configured to observe wavelengths close to the probe. The red-shifted EPW shares bandwidth with scattering from the 351 *nm* drive, so the EPW spectrometer observes blue shifted light in the range of 190 - 230 *nm*, capturing only the blue-shifted Langmuir waves traveling away from the target surface.

To analyze the data, the measured spectrum is fit with the power P_s of the Thomson scattered radiation[30] per solid angle $d\Omega$ and spectral width $d\omega$ with the scattering $\vec{k}$ determined by the geometry of the telescope.

$$\frac{dP_s}{d\Omega d\omega} = n_e L_{TS} P_{in} \frac{r_e^2}{2\pi} S(\vec{k}, \omega), \tag{1}$$

Here, r_e is the classical radius of an electron, c is the speed of light, P_{in} is the power of the probe, L_{TS} is the length of TS collection along the probe, and $S(\vec{k}, \omega)$ is the spectral density function,

$$S(\vec{k}, \omega) = \frac{2\pi}{k} \left| 1 - \frac{\chi_e}{\epsilon} \right|^2 \bar{f}_e \left(\frac{\omega}{k} \right) + \frac{2\pi}{k} \left| \frac{\chi_e}{\epsilon} \right|^2 \bar{Z} \bar{f}_i \left(\frac{\omega}{k} \right). \tag{2}$$

$$\chi_\alpha = \frac{\omega_{p\alpha}^2}{k^2} \int_{-\infty}^{\infty} \frac{1}{(\omega/k - v)} \frac{d}{dv} \bar{f}_\alpha(v) dv \tag{3}$$

where ω is the frequency shift applied to the scattered light, $\epsilon = 1 + \chi_e + \chi_i$ is the longitudinal dielectric function, and $\bar{Z}$ is the ionization state. $\bar{f}_i$ and $\bar{f}_e$ denote the velocity distribution functions of ions and electron respectively projected onto the direction of $\vec{k}$. This accurately describes the fluctuations in stable plasma, homogeneous at the scale of the scattering volume (here roughly $(100\mu m)^3$). Gradients in the plasma can be accounted for by integrating the power spectrum (1) over the scattering volume:

$$\frac{dP_s}{d\Omega d\omega} = \frac{r_e^2}{2\pi} \int n_e L_{TS} P_{in} S(\vec{k}, \omega) dV, \tag{4}$$

The EPW spectrum must also be multiplied by the wavelength-dependent sensitivity curve, based on the transmission of light in the OTS apparatus. Both spectra are then broadened by convolution with the instrument point spread function to account for the resolution of the measured spectrum.

When measuring the shape of the IAW, cf. Fig. 2c, it can be important to account for wavelength dependent broadening caused by the range of angles in the f/6.7 probe and f/10 collection volume [31]. This has two separable effects: changing the angle of $\vec{k}$ in the plasma, and changing the scattering angle, or equivalently, the size of $|\vec{k}|$. Since $\vec{k}$ is radial and nominally parallel to the flow in this experiment, changes in direction by a small angle have no significant effect on the spectrum.

Changes in $|\vec{k}|$, however, will shift each part of the spectrum, roughly in proportion to its phase velocity. This effect is detailed in [5].

The IAW spectrum is also affected by pulse front tilt due to the range of path lengths available to the scattered light in the spectrometer [21], [31]. This range of path lengths causes a measured IAW line out in time to be composed of a range of of times up to $95ps$ before or after the nominal time, with weighting falling off with a circular shape due to the smaller solid angles available for each larger time deviation.

The short time deviations caused by pulse front tilt primarily effect the IAW by widening the IAW peaks, as slowing flow velocities and cooling temperatures move the location of the resonance on the streak camera. This does not effect the total light captured from each IAW resonance, instead distributing this light to produce a lower, broader peak. Because the VFP profiles are created for discrete times where the immediate derivative of flow velocity cannot be seen, TS spectra account for pulse front tilt by adding additional smoothing to match the IAW peak width, which also preserves the total light in each IAW peak.

Equation (2) is valid for electron density fluctuation correlations at the wave vector $\vec{k}$ and frequency ω that evolve according to collisionless Vlasov theory and originate from discrete particle noise. For high-Z plasmas, evolution of the density fluctuations is modified by ion-ion (i-i) collisions even at the relatively high temperatures ($T_e = 1 - 2keV$) and modest densities of the plasma corona, $n_e \approx 10^{20} cm^{-3}$. Because of the high $Z \approx 50$ we have in such plasmas, $k\lambda_{ii} \approx 0.1$ where the wave number k corresponds to the density fluctuations that are tested in OTS and λ_{ii} is the i-i mean free path for thermal ions. At the same time electron collisions are negligible because $k\lambda_{ei} \gg 1$ and can be neglected when calculating $S(\vec{k}, \omega)$. The ion collisions, however, can change the asymmetry of the IAW peaks and are therefore crucial to the measurement of heat transport in high Z plasma.

A solution to the linearized dispersion relation for the IAW in the presence of particle collisions [22] has shown that the frequency of the IAW is well approximated by $\omega_s = \frac{kc_s}{\sqrt{1+k^2\lambda_{De}^2}}$ where $c_s = (ZT_e/m_i)^{1/2}$ for our parameters where $Z \gg 1$ (cf. Fig. 1 in Ref. [22]). Modifications of the IAW damping by i-i collisions are important, in fact, at $k\lambda_{ii} \approx 0.1$ ion damping is at the cusp of the transition between collisional and collisionless Landau damping (cf. Fig. 3 of Ref. [22]) and therefore a theory of $S(\vec{k}, \omega)$ requires proper treatment of the weakly collisional limit usually associated with nonlocal transport. The magnitude of the damping coefficient of the IAW due to ion collisions is small, comparable to electron Landau damping. In this experiment the broadening

of the ion-acoustic waves induced by damping falls below the resolution of the OMEGA IAW spectrometer, so the observed width of these features was dominated by the point spread function of the instrument.

The theory of plasma fluctuations is derived in Ref. [23] for arbitrary collision frequencies and particle noise sources. Because only i-i collisions are important for the fluctuations tested in OTS measurements of Au plasma, we approximate results of Ref. [23] by keeping collisional terms in ion response functions that are evaluated for the ion Maxwell distribution functions. All terms involving electron collisions are dropped and the dynamical form factor is given by the following expression:

$$S^c(\vec{k},\omega) = \frac{2\pi}{k}\left|1-\frac{\chi_e}{\epsilon^c}\right|^2 \bar{f}_e\left(\frac{\omega}{k}\right) + \frac{2}{\omega}\left|\frac{\chi_e}{\epsilon^c}\right|^2 \left(\frac{k}{k_{De}}\right)^2 Im[\chi_i^c]\frac{T_i}{T_e}, \tag{5}$$

where $\epsilon^c = 1 + \chi_e + \chi_i^c$ and $\chi_i^c(\vec{k},\omega)$ is the ion susceptibility function calculated with the effects of i-i collisions and defined by Eq. (28) of Ref. [23]. In the limit of collisionless ions $S^c(\vec{k},\omega)$ (5) takes the form of $S(\vec{k},\omega)$, Eq. (2).

Application of $S^c(\vec{k},\omega)$ (5) to the interpretation of the OTS spectra is important for the modeling of the ion peak asymmetry. While ion collisions do not shift the measured wavelengths of IAW peaks or modify their widths, the collisional damping does modify the relative amplitudes of the two peaks. Fig. 3 illustrates the effects of including i-i collisions on this asymmetry by comparing results with calculations using the collisionless $S(\vec{k},\omega)$ Eq. (2).

B. Radiation hydrodynamic simulations

The radiation hydrodynamic simulations presented here are described in detail in Refs. [4, 5], in which 2D simulations of uniformly illuminated gold spheres at intensities of $5 \times 10^{14} W/cm^2$ and 2 ns duration laser pulses are reported. Theses simulations predict temperature and density gradients in the plasma, which can be compared the the observed sing natures of heat transport.

Although ICF simulations typically reduce the incident laser power in simulations to match data (either observed bang-time, x-ray flux, or scattered light due to laser-plasma-interactions), it was found that using power multipliers to match the measured scattered light did not measurably change the plasma properties at the location of the TS probe. This allows conclusions regarding transport to be made even with a continued drive deficit [32]. Temperature and density profiles

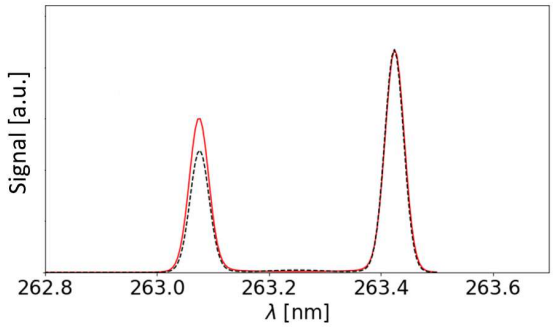

FIG. 3: IAW spectrum from gold plasma, Z=50, T_e=2 keV, T_i=1 keV, n_e=2.25×$10^{20} cm^{-3}$ and $v_e = -60 km/s$. The black dotted line shows the spectrum with no ion collisions, and the red line shows the spectrum including the effects of ion collisions, normalized to have the same peak amplitude.

of the ablating plasma are generated, shown in Fig. 4, with an ionization of $Z \approx 50$ for the gold plasma.

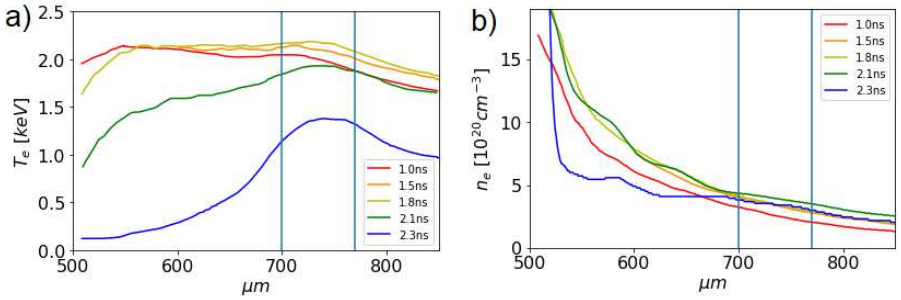

FIG. 4: Simulated electron temperatures (a) and electron density (b) from the SNB model as a function of the distance from the center of the sphere. Ionization remains near $Z = 50$ over most of the simulated profile. The extent of the probed region is marked by blue vertical lines. [Associated dataset available at https://doi.org/10.5281/zenodo.4951053] (Ref. [28]).

The plasma heating by the Thomson probe is included in the simulations. This is particularly important at the later times, t=2.1 ns, 2.3 ns when the main Omega laser beams are switched off and dense plasma cools rapidly outside the Thomson scattering volume due to radiation losses as

shown in Fig. 4a. Profiles of Figure 4 will be later reproduced by the analytical fits and used in Vlasov-Fokker-Planck simulations of the plasma in the TS volume in Sec. III C. All results of radiation-hydrodynamic simulations have been obtained using the SNB nonlocal transport model. These results can be compared to experimental data obtained from the OTS spectra at the probe location at 735 μm from the center of the sphere, between the vertical lines shown in Fig.4. These spectra can be fit to the observed IAW and EPW spectra (shown in Fig. 2), producing local measurements of the plasma at the probe location (Fig. 5). The fits to measured OTS spectra were obtained using OTS theory (4, 5) with Maxwellian electron and ion distribution functions.

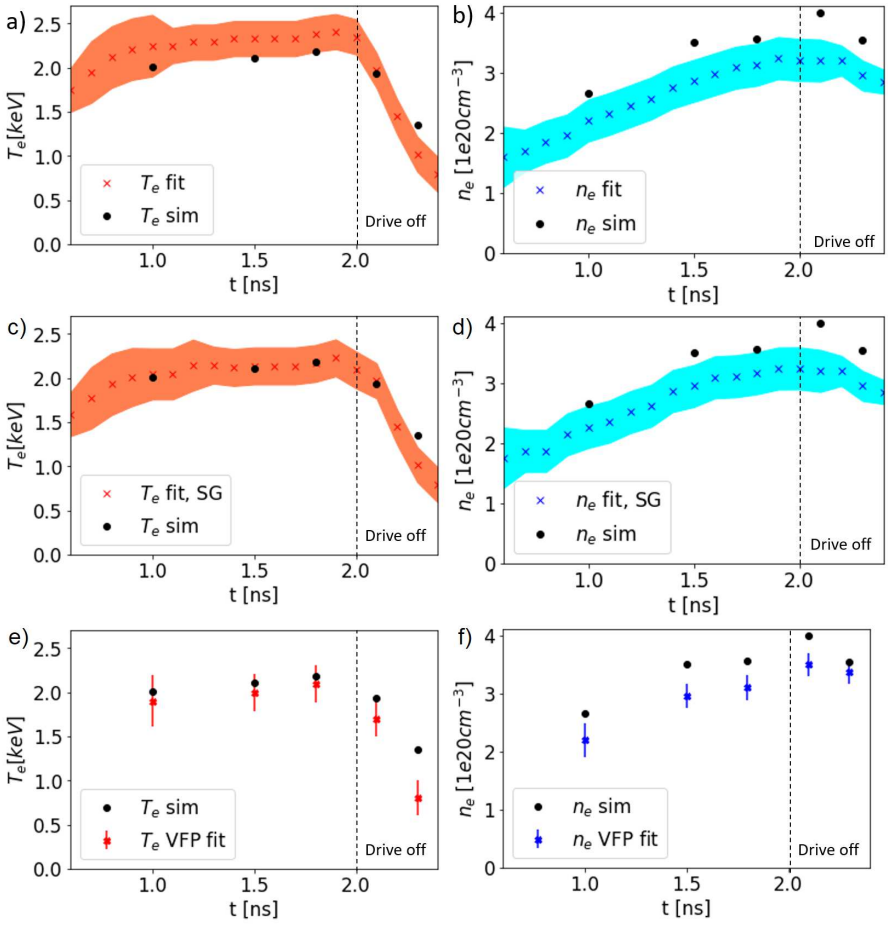

FIG. 5: Fits to the experimental OTS data (Fig. 2) assuming a Maxwell distribution for electrons (a, b), a super-Gaussian model (10) with m = 2.3 (c and d), and with VFP generated EDF shapes (e and f). Black dots are from radiation hydrodynamic simulations using SNB transport model. Absorption lines seen in the EPW spectrum may introduce additional uncertainly in the density measurements in the middle of the shot. The faster cooling and lower densities after the drive is off in all TS fits constitute a significant difference from the simulation. Super-Gaussian distributions are used up to 2 ns when the drive turns off.

III. HEAT FLUX MODELS

To measure the heat flow in the gold plasma using the OTS spectrum, we will follow an iterative procedure similar to the approach of Ref. [6]. In the collective regime of the OTS where we have measured IAW and EPW fluctuation spectra, the location of the IAW peaks is sensitive to electron temperature, flow velocity and the ion charge Z. Fitting of the EPW peak gives electron density and can verify electron temperature. Although simultaneous analysis of the results from EPW and IAW spectra can allow for the measurement of Z in the Au plasma [33], the simulated ionization of Z=50 is used here to reduce dependence on the EPW shape, which is sensitive to background light and density gradients in the TS volume (4). The EPW and IAW are fit together for T_e, n_e, flow velocity v_i, density gradients, and signal amplitude. Time evolution of these plasma parameters is consistent with radiation-hydrodynamic simulations [5] as is seen in Fig. 5. They are a starting point to the analysis below where we will examine various non-Maxwellian distribution functions corresponding to different thermal transport models. In this next approximation, different transport models are examined taking as the input these plasma parameters as well as the characteristic spatial profiles from radiation-hydrodynamic simulations, shown in Fig. 4.

Transport models can translate temperature profiles in space and time into the resulting distribution functions [6, 7]. To analyze the discrete time snapshots of the plasma conditions shown in Fig. 4, we have used heat transport models that are consistent with these conditions and can be compared with measurements. The perturbed EDFs relate the fast heat-carrying electrons to the resulting return current of slow electrons, which is measurable in ion acoustics wave spectra.

A. Spitzer-Härm heat flux

The Spitzer-Härm (SH) classical transport model [10] is valid in plasmas dominated by particle collisions and is derived from the Fokker-Planck kinetic equation in a current-free plasma with a temperature gradient, by expansion in the small parameter $\delta_T = \lambda_{ei}/L_T$ where $L_T = |\frac{d}{dx}\ln T_e|^{-1}$ is the temperature gradient scale length and λ_{ei} is the electron-ion mean free path. To the leading order in δ_T the electron distribution function is given by the perturbed local Maxwell distribution function:

$$f_{SH}(|\vec{v}|, v_x) = f_M(|\vec{v}|) + \sqrt{\frac{2}{9\pi}}(\frac{|\vec{v}|}{v_{T_e}})^4(4 - \frac{v^2}{2v_{T_e}^2})f_M(|\vec{v}|)\delta_T\frac{v_x}{|\vec{v}|}, \quad (6)$$

where $f_M(|\vec{v}|)$ is the Maxwell distribution, $v_{T_e} = \sqrt{T_e/m_e}$ and the gradient $\vec{\nabla} T_e$ is anti-parallel to the x-axis. The small parameter δ_T also determines the heat flux calculated using f_{SH} (6)

$$q_{SH} = \frac{m_e}{2} \int d^3v v_x v^2 f_{SH} = -\frac{128}{3\pi} n_e m_e v_{Te}^3 \delta_T \tag{7}$$

At $v > 2\sqrt{2} v_{T_e}$, fast heat carrying electrons enhance the tail of the distribution function in the direction opposite to the temperature gradient (6). At lower velocities the current produced by fast electrons is balanced with a cold return current. Given any δ_T, a sufficiently high velocity regime in f_{SH} (6) exists which will results in a negative distribution function indicating the break down of the expansion for fast particles with long mean free paths. Steep temperature gradients and long mean free paths corresponding to $\delta_T \geq 10^{-2}$ undo the local closure relation (7) and must be replaced by non-local heat transport models. For this reason, local hydrodynamic models often use flux-limited SH transport, where $q = min(q_{SH}, f q_f)$, with $q_f = n_e m_e v_{Te}^3$ and $f << 1$ (such a relation is illustrated later on in Fig. 10a).

The IAW spectra depend only on the low velocity electrons in the projected distribution function comprising the return current. This flow of electrons changes the damping of the IAW, (3) affecting the relative amplitudes of ion-acoustic resonances in the fluctuation spectra. This damping due to electrons can be described by the following relation (cf. e.g. Ref. [34]):

$$\gamma_e(k) = \sqrt{\frac{\pi}{8}} \frac{\omega_{pi}^2}{\omega_{pe}} \frac{k\lambda_{De}}{(1 + k^2\lambda_{De}^2)^2} \left[\frac{3}{2} \cos(\theta) \frac{k v_{Te}}{\omega_s} \delta_T - 1 \right], \tag{8}$$

where θ is the angle between k-vector and the temperature gradient, and $\omega_s = \frac{\omega_{pi}}{\sqrt{1+k^{-2}\lambda_{De}^2}} = \frac{k c_s}{\sqrt{1+k^2\lambda_{De}^2}}$ is the IAW frequency. This can be compared to the electron damping of IAWs caused by drifting Maxwellian electrons with $v_d = v_e - v_i$ (e.g. [35]):

$$\gamma_e(k) = \sqrt{\frac{\pi m_e}{8 m_i}} k \left(\frac{\omega_s}{k} - v_d \right). \tag{9}$$

By comparing Eqns. (8) and (9) one finds that the return current in the SH transport model can be accurately reproduced in the OTS spectra by a Maxwellian electron distribution function drifting at $v_d = 1.5 v_{Te} \delta_T$.

Depending on the sign of the phase velocity ω_s/k, the drift velocity v_d increases or decreases the electron Landau damping (9) creating asymmetry in the IAW resonances in the OTS spectra. In addition to electron damping terms these resonances are affected by the ion Landau damping,

very small for large Z plasma, and collisional damping due to i-i collisions. Collisions are included in the calculation of of the OTS spectra using $S^c(\vec{k},\omega)$ (5).

B. Non-Maxwellian EDFs due to IB heating and the electron thermal transport

In gold and other high-Z laser produced plasmas it is common to see evidence of super-Gaussian electron distributions,

$$f_{SG0}(|\vec{v}|) = \frac{m}{4\pi\Gamma(3/m)(\sqrt{2}v_m)^3} exp\left(-\left(\frac{|\vec{v}|}{\sqrt{2}v_m}\right)^m\right), \tag{10}$$

with $m > 2$, altering the spectral shape of the Thomson scattered light [14, 36, 37]. Here, v is the speed of the electrons and $v_m = \sqrt{\frac{3\Gamma(3/m)}{2\Gamma(5/m)}}v_{T_e}$, $v_{T_e} = \sqrt{T_e/m_e}$. This super-Gaussian distribution function arises due to competition between IB heating, which evolves the EDF towards the super-Gaussian distribution [24] and electron-electron collisions which thermalize the plasma. EDF (10) was derived in Ref. [38] from the results of Fokker-Planck simulations. For homogeneous laser-heated plasma, Ref. [38] includes a practical expression for the exponent $m(\alpha) = 2 + \frac{3}{1+1.66\alpha^{-0.724}}$ where $\alpha = Z(v_{osc}/v_{Te})^2$, and v_{osc} is the oscillatory velocity of electrons in the electric field of the laser. For our experiment, the super-Gaussian exponent at the OTS probe location is limited to $m \leq 2.3$ by this relation, based on the intensity of the 3 ω drive [38]. For the EPW, this small change in the electron distribution function has an insignificant effect given the noise present in the measured spectrum. The IAW spectrum responds to the shape of the electron distribution function at $|\vec{v}| << v_{Te}$, so larger super-Gaussian coefficients appear to fit OTS spectra with slightly lower electron temperatures. This is illustrated in Fig. 5c,d where we compared time evolution of electron temperature and density from the OTS spectra fitted using EDF $f_{SG0}, m = 2.3$ (10) with the radiation-hydrodynamic results. Successive improvements of the fits to the OTS spectra as we gain a better understanding of the kinetic processes underlining the evolution of the plasma are part of the overall strategy of our OTS experiments. More precise subtraction of the noise in the EPW spectra during planned new experiments with background shots will help to identify effects of the super-Gaussian distribution functions.

When a super-Gaussian electron distribution function is present, IAW resonance frequencies are increased slightly, and heat transport is significantly affected [8, 9]. The perturbation solution to the Fokker-Planck kinetic equation by expansion in parameters δ_T and $\delta_n = \lambda_{ei}\frac{d}{dx}\ln(n_e)$ about super-Gaussian background distribution results in the following electron distribution function

$$f_{SG}(|\vec{v}|, v_x) = f_{SG0}(|\vec{v}|) + f_{SG0}(|\vec{v}|)\frac{v_x}{|\vec{v}|}\left(\frac{|\vec{v}|}{\sqrt{2}v_{T_e}}\right)^4 \left(\left(\frac{m}{2}\left(\frac{|\vec{v}|}{\sqrt{2}v_m}\right)^m - \frac{5m}{12}\frac{\Gamma(8/m)}{\Gamma(6/m)}\left(\frac{|\vec{v}|}{\sqrt{2}v_m}\right)^{m-2}\right)\delta_T - \left(\frac{m}{6}\frac{\Gamma(8/m)}{\Gamma(6/m)}\left(\frac{|\vec{v}|}{\sqrt{2}v_m}\right)^{m-2} - 1\right)\delta_n\right), \tag{11}$$

that is an equivalent of the SH theory (6) for the super-Gaussian distribution. Increasing the super-Gaussian coefficient m reduces the effects of temperature gradients on the heat flux in a plasma [39] (as is shown in Fig. 6a) and also results in contributions to closure relation that are proportional to density gradients [8, 27, 40], with thermal energy flowing towards the higher density region,

$$q/q_f = (q_T + q_n)/q_f = -K_T\delta_{T_e} - K_n\delta_n, \tag{12}$$

where the transport coefficients can be written as

$$\begin{aligned} K_T &= \sqrt{\frac{2}{9\pi}}a(7b - 5c) \\ K_n &= \sqrt{\frac{2}{9\pi}}2a(b - c) \end{aligned} \tag{13}$$

with $a = \Gamma(3/m)^{5/2}(\frac{3}{\Gamma(5/m)})^{7/2}$, $b = \frac{\Gamma(10/m)}{12}$ and $c = \frac{\Gamma(8/m)^2}{9\Gamma(6/m)}$ [8] [41]. For ablating plasmas where temperature and density gradients both point towards the target, this results in a decreased heat flux when compared to Spitzer-Härm.

Transport theory with the super-Gaussian distribution leads to closure relations for the heat flux that involve gradients of density and temperature. In the final analysis of this paper, this will show the trends that lead to better agreement between theory and experimental measurement.

C. Vlasov-Fokker-Planck simulations

As described above in Sec. III A the classical SH transport model can work well in plasmas where the characteristic parameter $\delta_T < 10^{-2}$ [42] and for larger temperature gradients it has to be replaced by the kinetic description in terms of Vlasov-Fokker-Planck (VFP) simulations [43] or nonlocal transport models [26]. The nonlocal transport, so called SNB [26] model has been used in the radiation hydrodynamic description of the Au plasma [5] and led to accurate modeling of the

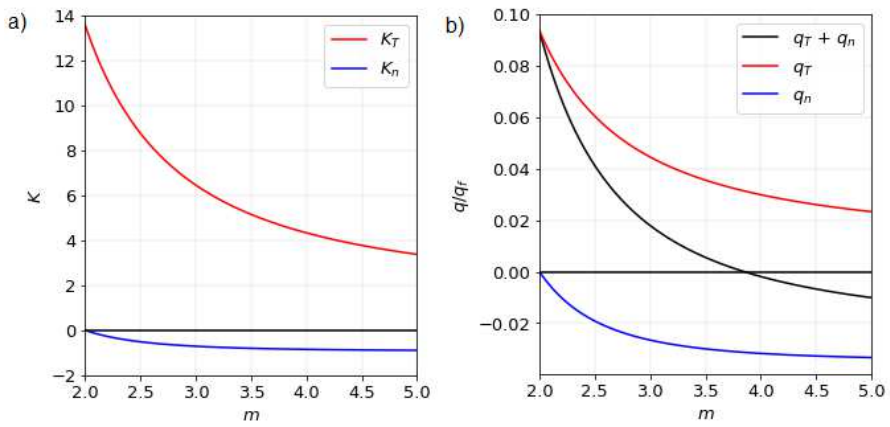

FIG. 6: a) Heat transport coefficients in super-Gaussian plasma: $q/q_f = -K_T\delta T_e - K_n\delta_n$, (13) b) Heat transport due to temperature and density gradients in super-Gaussian plasma found using profiles for t=1ns as seen in Fig. 4, shown as a fraction of $q_f = n_e m_e v_{Te}^3$

electron temperature and density evolution, cf. Fig. 5e,f. We have used density and temperature profiles from the radiation hydrodynamic simulations with SNB transport in VFP simulations with the K2 code [7]. VFP simulations were performed in the relatively small OTS volume and usually quickly converged to a quasi-stationary solution for the electron distribution function. This has been expected as the VFP has been consistent with the SNB model [7] in the broad range of plasma parameters. We will use the density and temperature profiles from the nonlocal rad-hydro simulations [5] as input to Vlasov-Fokker-Planck (VFP) simulations with the K2 code [7]. In order to initialize the K2 simulations, we first generate analytic fits to the SNB profiles seen in Fig. 4 for electron temperature and density, respectively (Fig. 7):

$$\frac{T_e(r)}{keV} = \frac{T_H - T_L}{2}\tanh\left(\frac{r+5\mu m}{75\mu m}\right) + \frac{T_H + T_L}{2} + p_0\tanh\left(\frac{r-p_1\mu m}{p_2\mu m}\right), \tag{14}$$

$$\begin{aligned}\frac{n_e(r)}{10^{20}cm^{-3}} = N_H + \frac{q_0}{2}(1+\tanh\left(\frac{r+210\mu m}{7.5\mu m}\right))exp(\frac{-q_1 r}{\mu m}) \\ +(1-0.5(1+\tanh\left(\frac{r+210\mu m}{7.5\mu m}\right)))(N_L - N_H)\end{aligned} \tag{15}$$

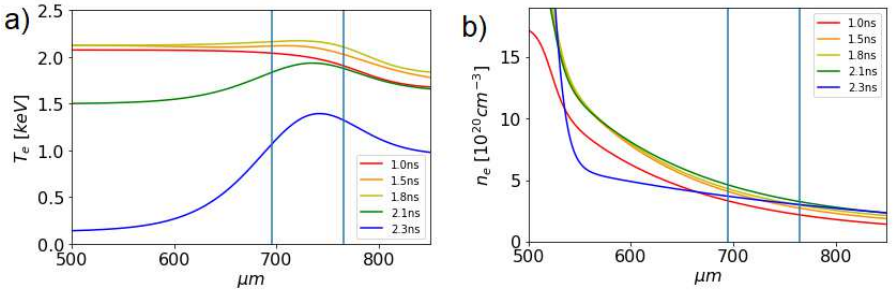

FIG. 7: Fits (14, 15) to the simulated temperatures (a) and density (b) profiles seen in Fig. 4, which can be extended further in radius to account for non-local effects. Vertical lines show the limits of the TS volume where the TS probe beam is pointed, which contributes some plasma heating at later times.

where T_H, T_L, and p_{0-2} are fit from the temperature profile and N_H, N_L, and q_{0-1} are fit from the density profile.

Once the density and temperature is set, K2 is run iteratively on r=0μm to r=1500μm until a steady-state heat-flux is produced which is consistent with the profiles. IB heating is applied from the drive and probe beams, and the initial temperature profile is maintained in K2 by external heating and cooling operators. The electron distribution function is otherwise permitted to evolve self-consistently along with the electric field. The heating and cooling operators increase or decrease the temperature in a manner that produces a symmetric distribution, f_{0VFP}, with some super-Gaussian characteristics (Fig. 8a), with anti-symmetric perturbations, f_{1VFP}, creating heat flux. This f_1 distribution also shows some super-Gaussian effects, including the reversal of the transport direction at low velocities seen in higher exponent super-Gaussians in the presence of density gradients (Fig. 8b). The distribution function can then be sampled anywhere along the profile to see the resulting form $f_{1VFP}(v)$ of the heat carrying electrons and the return current. These profiles typically carry heat at velocities lower than the Spitzer-Härm distribution (6), resulting in a relatively small ratio of heat flux to return current (seen later in Fig. 10). For the application of VFP simulations to be valid, we are implicitly assuming the temperature profile produced by the SNB model is not too different to the temperature profile that would be generated by a fully self-consistent VFP simulation. Such full VFP simulations are still beyond our modeling capabilities. The heating operator is of the Langdon form [24], which is important to produce the correct super-

Gaussian exponent for the symmetric part of the electron distribution [38]. The cooling operator, which accounts for the cooling terms in the radiation hydrodynamic simulations such as radiative cooling and PdV work [44], is a modified Langdon operator that generates a cooler Maxwellian distribution (in the absence of other processes).

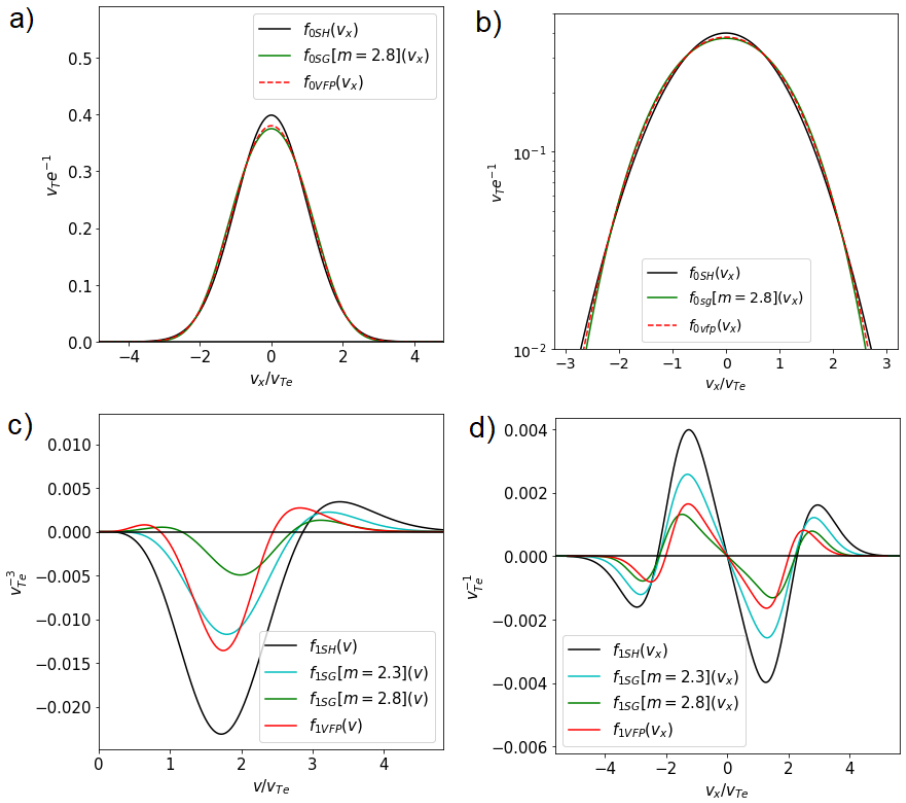

FIG. 8: Electron distribution functions in the center of the OTS scattering region in the simulated profiles (Fig. 4) at 1ns, Te=2.03keV are displayed. f0 is shown in linear (a) and log scale (b), and f1 is displayed in (c) and (d) on $|v|$ and projected onto the scattering direction respectively. Spitzer-Härm (black), VFP (red), the expected super-Gaussian of m=2.3 (blue) and an m=2.8 super-Gaussian (green) are shown. Inversion in the return current due to density gradients can be seen in (c) for the m=2.8 super-Gaussian and the VFP distribution function.

The VFP generated distribution functions can also be used to fit the observed TS spectra (Fig. 5e,f). In this case the shape of the electron distribution is taken from the simulations, but the width and amplitude is fit to match the TS spectra. This results in temperatures fairly similar to the simulated temperatures before the drive is off, with an RMS error of 107ev. This can also be seen in the IAW from unchanged VFP spectra shown at the simulated temperature (Fig. 9).

IV. HEAT FLUX MEASUREMENTS

OTS has been established as the routine diagnostic of plasma parameters such as density, temperature, flow velocity. Additionally, because the dynamical form factors $S(\vec{k},\omega)$ (2) and $S^c(\vec{k},\omega)$ (5) are expressed in terms of the particle distribution functions they can be used to study non-equilibrium plasmas characterized by the super-Gaussian or distribution functions with nonzero heat fluxes. Analysis in this section is focused on the asymmetry of the ion-acoustic peaks in the low-frequency OTS spectrum (cf. Figs 3, 9) caused by the electron distribution functions with non-zero heat flux [18].

Asymmetry in the ion-acoustic resonances can be produced by a current flowing in the plasma [15, 16], or by a return current of low velocity electrons (shown in Fig. 8). Return current is necessary to cancel the current of fast, heat carrying electrons in a plasma with nonzero heat flux. Both of these electron distribution functions have a similar effect on the observed IAW (cf. e.g. Eqns. (8) and (9) and discussion in Sec. III A). In our spherically symmetric experiments the geometry justifies an assumption of no significant magnetization of the plasma outflow. This allows us to restrict ourselves to investigating zero-current distribution functions in order to explain the IAW asymmetry.

We begin by fitting IAW spectra using SH distribution function (6) over the full time duration of the OTS probe. Results of this fit are displayed in Fig. 10a in terms of the electron heat flux (7) by black dots within the gray background indicating errors in the measurements. Plasma is assumed to be spherically symmetric with radial temperature gradient producing the Spitzer-Härm parameter $\delta_T = \lambda_{ei}\frac{d}{dx}\ln(T_e)$ at each moment in time. This parameter is fit to the asymmetry of the IAW resonances (seen in the raw experimental data of Fig. 2 and in Fig. 9). The resulting particle heat flux away from the sphere at 735μm grows from 0 after $\approx$ 1ns, reaching $0.4TW$ before reversing direction at 2ns when the drive is off, cf. Fig. 10a. Figure 10a includes our main theoretical results, red crosses, i.e. heat flux calculated using electron distribution functions from the VFP simulations

in the OTS volume with the temperature (14) and density (15) profiles obtained in radiation-hydrodynamic simulations (cf. Figs. 4 and 7). By comparison to these results, interpretation of the OTS measured heat flux uses temperatures and densities from the basic OTS measurements, Figs. 5a,b, and the heat flux is evaluated from the properties of the experimental spectra using the Spitzer-Härm EDF and with no input from the radiation-hydrodynamic simulations.

We have also compared this largely experimental measurement of the SH heat flux to the results of radiation-hydrodynamic simulation where the SH heat flux is calculated from the gradients given by the analytical fits of the profiles, Eqns. (14), (15), Fig. 7 (section III A). These gradients are averaged over the probed region, weighting by laser area and plasma density. The mean free-path over scale lengths from these profiles for $t = (1.0, 1.5, 1.8, 2.1, 2.3) ns$ are $\delta T = (-0.00689, -0.00442, -0.00296, -0.000261, 0.00381)$ and $\delta n = (-0.0373, -0.0320, -0.0291, -0.0205, -0.00744)$ (12). The resulting SH heat flux (large red dots, Fig. 10a) shows a similar reversal around the drive turn-off, but there are large discrepancies with the experimental SH based measurement (black), which can be seen in Fig. 10a. Other EDFs, however, cannot be compared to this result since similar transport could still produce differing IAW asymmetries. The physical processes included in the radiation-hydrodynamic simulations, such as the nonlocal transport model, SNB [26] and the atomic physics, are incompatible with a simple SH theory of thermal transport.

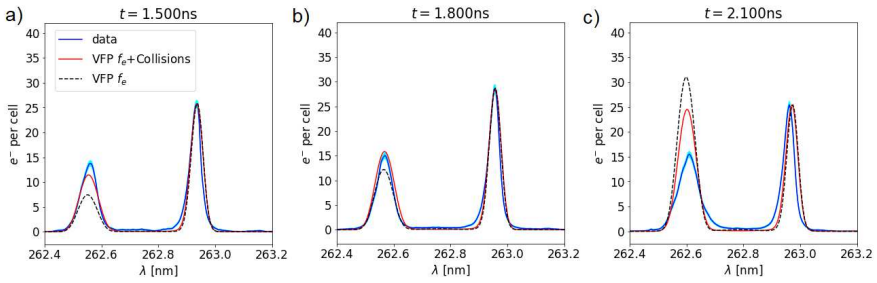

FIG. 9: IAW data (blue) in photo-electrons produced per ccd cell, and spectra from VFP EDFs with collisions (red) and without collisions (black). Flow velocity is fit to the IAW data while all other parameters are generated from the simulated profiles (Fig. 7). Figures a) and b) show good agreement with temperature (Seen in IAW separation) before the drive is turned off at 2ns.

A more inclusive approach to comparing experimental results and theories is shown in Fig. 10b where we plot a ratio of areas under the blue and the red shifted IAW peaks in the OTS spectra - blue continuous line with the light blue background defining errors inherent in the streak camera's light detection. This allows all the EDF asymmetries to be compared to the observed IAW. These experimental results are well reproduced by the VFP simulations (cf. Figs. 9) and the radiation-hydrodynamic generated density and temperature profiles at $t \geq 1.5ns$ and the simulated SH IAW spectra at $t \geq 1.8ns$.

To create the VFP-based IAW spectrum, discussed above, six electron distribution functions from different locations in the OTS volume are used to construct OTS spectra, which are then averaged weighting by probe area and electron density. The resulting IAW spectrum has asymmetry corresponding to the heat transport processes in the Vlasov-Fokker-Planck simulation. As shown in Figs. 9 and 10b, these are mostly consistent with the OTS data, with the exception of t=1ns where no significant asymmetry is detected in the experiment.

The surprising result in Fig. 10 is the almost complete disappearance of the heat flux early in time $t \leq 1ns$ in the OTS volume. This is illustrated by the lack of asymmetry in IAW peaks in Fig. 10b and in the corresponding blue peak fraction ≈ 0.5 in the experimental asymmetry in Fig. 10b. Reduction of the heat flux would have to be significantly larger than the limit given by $f = 0.03$ and plotted for comparison in Fig. 10a to reproduce these results. The free streaming flux q_f limited by $f = 0.03$ agrees with VFP calculations at t=1 ns but it differs from experimental measurement of IAW peak asymmetry at that time. Note, that macroscopic theories of ICF plasmas [2, 3] have identified a need for changing flux inhibitors during plasma evolution and for strongly reduced transport early during the interaction while the late time evolution was correctly described by the SH model.

The lack of asymmetry in the IAW resonances at 1 ns shows a significant discrepancy with both the SH and VFP electron particle distribution functions. This failure of radiation hydrodynamic simulations in obtaining correct particle transport happens in spite of a reasonable agreement between measured and simulated temperatures and densities at early times. Although closer examination of the time evolution of these parameters, cf. Figs. 8 and 9 in Ref. [5], shows different increase rates of electron densities and temperatures early in time. Further observation has been provided by the ongoing campaign in Be plasmas where no such initial disappearance of the heat fluxes has been observed, thus suggesting that some ionization-dependent and specific to high-Z plasmas processes such as radiation transport or super-Gaussian distributions may be causing this

discrepancy.

If high super-Gaussian exponents are used in the fits of the OTS spectra, the disappearance of the heat flux could be explained by the effect of the density gradient as shown in the local transport theory (12), (13). To match the early time OTS data using local transport closures, $m \approx 3.8$ is required to eliminate asymmetry in the ion-acoustic resonances and reduce to zero thermal flux, as seen in Fig. 6b. However, such a high m-coefficient would significantly alter the results of the OTS fits for temperature and density. Note that f_{SG} (11) $m = 2.3$, which is consistent with the formula $m(\alpha)$ of Ref. [38], changes $T_e(t)$ and $n_e(t)$ by more than 10% as demonstrated in Figs 5c and d, but has a small effect on the heat flux calculations, cf. Fig. 10 b. However, calculated super-Gaussian exponents as well as the IB effects in the VFP distributions use a smooth laser intensity in space for the probe and heating beams. It is therefore possible that beam speckles may lead to higher-m super-Gaussian electron distributions, as the TS signal will disproportionately come from higher intensity speckles in the probe. We can see that the direct effects of such a distribution would be to reduce heat flux and improve the agreement with the data (Fig. 10 b), but an analysis of the full effect of this would require large-scale kinetic simulations to justify its existence, since the SNB simulations used to construct the temperature and density gradients do not use super-Gaussian effects on heat transport.

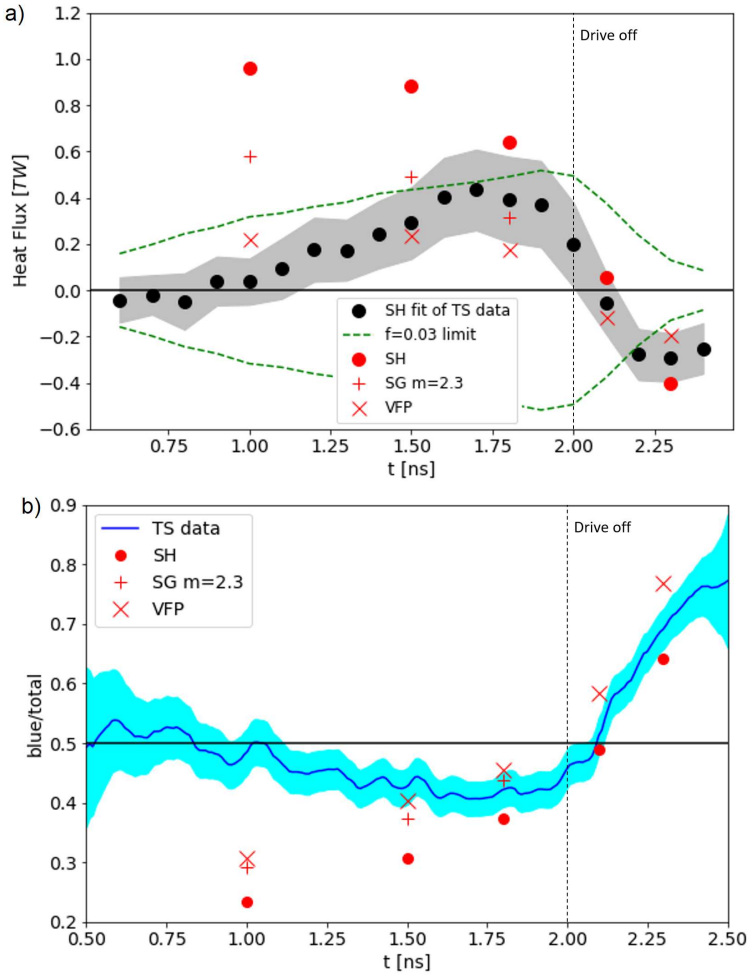

FIG. 10: Electron heat flux out of the spherical target (a) and asymmetry of the ion acoustic wave (b). Various transport models applied to the simulated plasma profiles (Fig. 4) are shown in red. (a) shows heat flux found with SH fits to TS data in black. A commonly used flux limiter of f=0.03 is shown in green in figure (a) for comparison. (b) shows the asymmetry of the IAW in blue, plotted as the integrated detected signal in the blue-shifted peak divided by the total IAW signal. The shaded error region represents the statistical error of the photo electrons appearing in each IAW feature.

V. SUMMARY AND CONCLUSIONS

Using OTS spectra from a spherically symmetric direct-drive experiment, we have made detailed measurements of the electron return current and the related electron heat flux. This work has been a part of ongoing experimental campaigns [4, 5] where OTS measurements in Be and Au plasmas have been used to validate transport models in the radiation-hydrodynamic simulations. The following strategy is realized in the application of the OTS data to measure electron temperature, density and flow velocity in the Au plasma. Figures 5a,b show the time evolution of T_e and n_e from the basic interpretation of the OTS spectra using Maxwell distribution functions and the OTS theory based on the collisionless $S(\vec{k},\omega)$ (2), plasma response functions (3) and the scattered power averaged over the OTS volume (4). These results are compared with the large-scale radiation hydrodynamic simulations (black dots) [5] over the time duration of the OTS probe. Parameters of Fig. 5 and spatial profiles from radiation-hydrodynamic simulations, Fig. 4 are used in the subsequent applications of different transport theories, improved form factor models (5) and solutions to VFP kinetic equations. We have verified in Fig. 5 that new distribution functions such as the super-Gaussian (10) or the solutions to the VFP equations improve the accuracy of OTS fits and suggest convergence of the successive approximations to the OTS spectra with more complete models of the electron distribution functions resulting in better matches to the experimental parameters.

The main result of our paper is a calculation of the electron heat flux from the asymmetry of the ion-acoustic resonances in the low-frequency part of the OTS spectrum (cf. Fig. 2 c). Such a program of describing electron heat transport was realized in Refs. [6] and [18] using asymmetry of the EPW or IAW peaks. Application of the IAW spectrum poses unique challenges of the correct accounting of the spectral shape including instrumental effects [29, 31] that contribute to different amplitudes of ion-acoustic resonances [5]. Also, modelling of hot Au plasma provides a set of difficult challenges, especially in combining a radiation cooling operator with the VFP code. Because of high ionization, $Z = 50$, ion-ion collisions dominate the damping of the IAW fluctuations and have to be included in the theory of the form factor $S^c(\vec{k},\omega)$ (5). We have followed a conclusion of the previous study [7] and assumed that the SNB nonlocal transport model [26] used in the radiation-hydrodynamic code gives results that are consistent with solutions of the VFP kinetic equations. This has allowed the application of the density and temperature profiles from radiation hydrodynamic simulations, Fig. 7, in the VFP calculations to obtain EDFs that are used in the evaluation of the dynamical form factor $S^c(\vec{k},\omega)$ (5) and the OTS spectra.

From the fits of the OTS spectra, we have obtained electron heat flux shown in Fig. 10 a. The characteristic of the OTS spectra that is directly measured is the asymmetry of the IAW resonances, cf. Fig. 10 b. The heat flux and asymmetry of ion-acoustic resonances have been compared with the VFP model EDF solutions, as well as theoretical results employing EDFs from the SH transport theory (6) and local transport theory based on the super-Gaussian EDF (11). Super-Gaussian induced limitations on heat transport are not included in the simulated SNB profiles, so the super-Gaussian results are included to show the direct effects of this EDF at the probe location. The most accurate are results obtained from the VFP model (red crosses in Fig. 10) that includes nonlocal transport and the modifications of the EDF due to the inverse Bremsstrahlung heating. For the latter half of the OTS probe duration, they are consistent with the radiation hydrodynamic and SNB results. The latter deviates from the SH theory for $t \leq 1.8ns$, underscoring the importance of the nonlocal transport effects in our experiment. At the late time, $t = 2.3ns$ radiation cooling dominates plasma evolution even in the low-density part of the plasma corona where the OTS measurements are taken. An approximate form of the cooling operator in the VFP theory contributes to the discrepancy from the SNB and complex atomic physics models in the radiation hydrodynamic modelling at this late time.

Significant deviations in the measured heat flux between simulations and OTS data are seen shortly after the plasma is fully heated to roughly 2 keV. Measurements at $t = 1ns$ show an almost complete disappearance of the asymmetry in IAW resonances and the dramatic reduction in the electron heat flux. None of the theoretical models were able to capture these effects within constraints provided by the temperature and density profiles from the radiation hydrodynamics simulations. The higher exponents in the super-Gaussian EDF and related transport theory may have desirable effects due to cancellations between terms proportional to density and temperature gradients. As high density gradients are expected to be prevalent closer to the critical surface, this super-Gaussian transport limitation may play an important role in heat transport closer to the target surface early on in the shot, potentially affecting laser coupling and plasma in the OTS volume further in the corona. Restricting heat flux early on in laser shots within hydrodynamic models has been proposed to match experiments before [2, 3], and it is possible that this need for limited flux could be explained by super-Gaussian transport effects.

VI. ACKNOWLEDGMENTS

This work was performed under the auspices of the U.S. Department of Energy by Lawrence Livermore National Laboratory (LLNL) under Contract DE-AC52-07NA27344. This work was supported by LLNL's WPD ICF Program's Academic Collaboration Teams's University Program (ACT-UP) under subcontract B645970.

VII. DATA AVAILABILITY

The data that support the findings of this study are openly available in Zenodo at https://doi.org/10.5281/zenodo.4950678, reference number [28].

[1] M. A. Barrios, J. D. Moody, L. J. Suter, M. Sherlock, H. Chen, W. Farmer, J. Jaquez, O. Jones, R. L. Kauffman, J. D. Kilkenny, et al., Physical Review Letters **121**, 095002 (2018).

[2] M. Rosen, H. A. Scott, D. E. Hinkel, E. Williams, D. Callahan, R. Town, L. Divol, P. A. Michel, W. L. Kruer, L. J. Suter, et al., High Energy Density Physics **7**, 180 (2011).

[3] M. D. Rosen, Bull. Am. Phys. Soc. 63 (11), UP11.00107, 60th Annual Meeting of the APS Division of Plasma Physics, Portland, OR. (2018).

[4] W. A. Farmer, C. Bruulsema, G. F. Swadling, M. W. Sherlock, M. D. Rosen, J. S. Ross, and W. Rozmus, Phys. Plasmas **27**, 082701 (2020).

[5] W. A. Farmer, M. D. Rosen, G. F. Swadling, C. Bruulsema, C. D. Harris, W. Rozmus, M. B. Schneider, M. W. Sherlock, D. H. Edgell, J. Katz, et al., Phys. Plasmas **28**, 032707 (2021).

[6] R. Henchen, M. Sherlock, W. Rozmus, J. Katz, D. Cao, J. Palastro, and D. Froula, Physical Review Letters **121**, 125001 (2018).

[7] M. Sherlock, J. P. Brodrick, and C. P. Ridgers, Physics of Plasmas **24**, 082706 (2017).

[8] P. Mora and H. Yahi, Phys. Rev. A. **26**, 4 (1982).

[9] S. Brunner and Valeo, Physics of Plasma **9**, 923 (2002).

[10] L. Spitzer and R. Härm, Phys. Rev. **89**, 977 (1953).

[11] J. Ross, H.-S. Park, R. Berger, L. Divol, N. Kugland, W. Rozmus, D. Ryutov, and S. H. Glenzer, Physical Review Letters **110**, 145005 (2013).

[12] A. L. Milder, J. Katz, R. Boni, Palastro, Sherlock, W. Rozmus, and D. H. Froula, Phys. Rev. Lett. **127**, 015001 (2021).

[13] A. L. Milder, H. P. Le, M. Sherlock, P. Franke, J. Katz, S. T. Ivancic, J. L. Shaw, J. P. Palastro, A. M. Hansen, W. Rozmus, et al., Phys. Rev. Lett. **124**, 025001 (2020).

[14] S. H. Glenzer, K. G. Estabrook, R. W. Lee, B. J. MacGowan, and W. Rozmus, JQSRT **65**, 253 (2000).

[15] G. Swadling, C. Bruulsema, F. Fiuza, D. Higginson, C. Huntington, H.-S. Park, B. Pollock, W. Rozmus, D. Ryutov, H. Rinderknecht, et al., Physical Review Letters **124**, 215001 (2020).

[16] C. Bruulsema, W. Rozmus, G. Swadling, S. Glenzer, H.-S. Park, J. Ross, and F. Fiuza, Physics of Plasmas **27**, 052104 (2020).

[17] G. Gregori, S. Glenzer, J. Knight, C. Niemann, D. Price, D. H. Froula, M. J. Edwards, R. P. J. Town, A. Brantov, W. Rozmus, et al., Physical Review Letters **92**, 205006 (2004).

[18] J. Hawreliak, D. M. Chambers, S. H. Glenzer, A. Gouveia, R. J. Kingham, R. S. Marjoribanks, P. A. Pinto, O. Renner, P. Soundhauss, S. Topping, et al., J. Phys B: At. Mol. Opt. Phys. **37**, 1541 (2004).

[19] Q. Z. Yu, Y. T. Li, S. M. Weng, Q. M. Dong, L. F., Z. Zhang, J. Zhao, X. Lu, C. Danson, D. Pepler, et al., Physical of Plasma **17**, 043106 (2010).

[20] S. H. Glenzer, W. E. Alley, K. G. Estabrook, J. S. De Groot, M. G. Haines, J. H. Hammer, J.-P. Jadaud, B. J. MacGowan, J. D. Moody, W. Rozmus, et al., Physics of Plasmas **6**, 2117 (1999).

[21] J. Katz, R. Boni, R. Rivlis, C. Muir, and D. H. Froula, Review of Scientific Instruments **87**, 11E535 (2016).

[22] A. Brantov, V. Y. Bychenkov, and W. Rozmus, Phys. Rev. Lett. **108**, 205001 (2012).

[23] W. Rozmus, A. Brantov, C. Fortmann-Grote, V. Y. Bychenkov, and S. Glenzer, Phys. Rev. E. **96**, 043207 (2017).

[24] A. B. Langdon, Phys. Rev. Lett. **44**, 575 (1980).

[25] D. Turnbull, A. Colaïtis, A. M. Hansen, A. L. Milder, J. P. Palastro, J. Katz, C. Dorrer, B. E. Kruschwitz, D. J. Strozzi, and D. H. Froula, Nature Physics **16**, 181 (2020).

[26] G. P. Schurtz, P. D. Nicolaï, and M. Busquet, Phys. Plasmas **7**, 4238 (2000).

[27] C. P. Ridgers, A. G. R. Thomas, R. J. Kingham, and A. P. L. Robinson, Physics of Plasma **15**, 092311 (2008).

[28] C. Bruulsema, W. A. Farmer, M. Sherlock, G. Swadling, M. Rosen, S. Ross, and W. Rozmus, *Characterization of thermal transport and evolution of au plasma in icf experiments by thomson scattering - ts data*, `https://doi.org/10.5281/zenodo.4951053` (2021).

[29] J. Katz, R. Boni, C. Source, R. Follett, M. J. S. III, and D. H. Froula, Review of Scientific Instruments **83**, 10E349 (2012).

[30] D. H. Froula, S. H. Glenzer, N. C. Luhmann, and J. Sheffield, *Plasma Scattering of Electromagnetic Radiation: Theory and Measurement Techniques* (Elsevier, 20011).

[31] R. K. Follett, J. A. Delettrez, D. H. Edgell, R. J. Henchen, J. Katz, J. F. Myatt, and D. H. Froula, Review of Scientific Instruments **87**, 11E401 (2016).

[32] J. D. Moody, D. A. Callahan, D. E. Hinkel, P. A. Amendt, K. L. Baker, D. Bradly, P. M. Celliers, E. L. Dewald, L. Divol, T. Döppner, et al., Physical of Plasma **21**, 056317 (2014).

[33] S. H. Glenzer, W. Rozmus, B. J. MacGowan, K. G. Estabrook, J. S. De Groot, G. Zimmerman, H. Baldis, J. A. Harte, R. Lee, E. A. Williams, et al., Physical Review letters **82**, 97 (1999).

[34] A. Brantov, V. Y. Bychenkov, and W. Rozmus, Physics of Plasma **8**, 3558 (2001).

[35] S. Ichimaru, *Basic Principles of Plasma Physics - A Statistical Approach* (W.A. Benjamin, Reading, 1973).

[36] E. Fourkal, V. Y. Bychenkov, W. Rozmus, R. Sydora, C. Kirkby, C. E. Capjack, S. H. Glenzer, and H. A. Baldis, Phys. Plasma **8**, 550 (2001).

[37] A. L. Milder, H. P. Le, M. Sherlock, P. Franke, J. Katz, S. T. Ivancic, J. L. Shaw, J. P. Palastro, A. M. Hansen, I. A. Bergishev, et al., Phys. Rev. Lett. **124**, 025001 (2020).

[38] J. P. Matte, M. Lamoureux, C. Moller, R. Y. Yin, J. Delettrez, V. J., and T. W. Johnston, Plasma Phys. Contr. Fusion **30**, 1665 (1988).

[39] A. S. Joglekar, C. P. Ridgers, R. J. Kingham, and A. G. R. Thomas, Phys. Rev. E. **93**, 043206 (2016).

[40] J. J. Bissell, C. P. Ridgers, and R. J. Kingham, New Journal of Physics **15**, 025017 (2013).

[41] A. Brantov, V. Y. Bychenkov, and W. Rozmus, Plasma Physics Reports **32**, 337 (2006).

[42] E. M. Epperlein, Physics of Plasmas **1**, 109 (1994).

[43] A. Bell, R. G. Evans, and D. J. Nicholas, Physical Review letters **46**, 243 (1981).

[44] G. Bekefi, *Radiation Processes in Plasmas* (J. Wiley and Sons, New York, 1966).

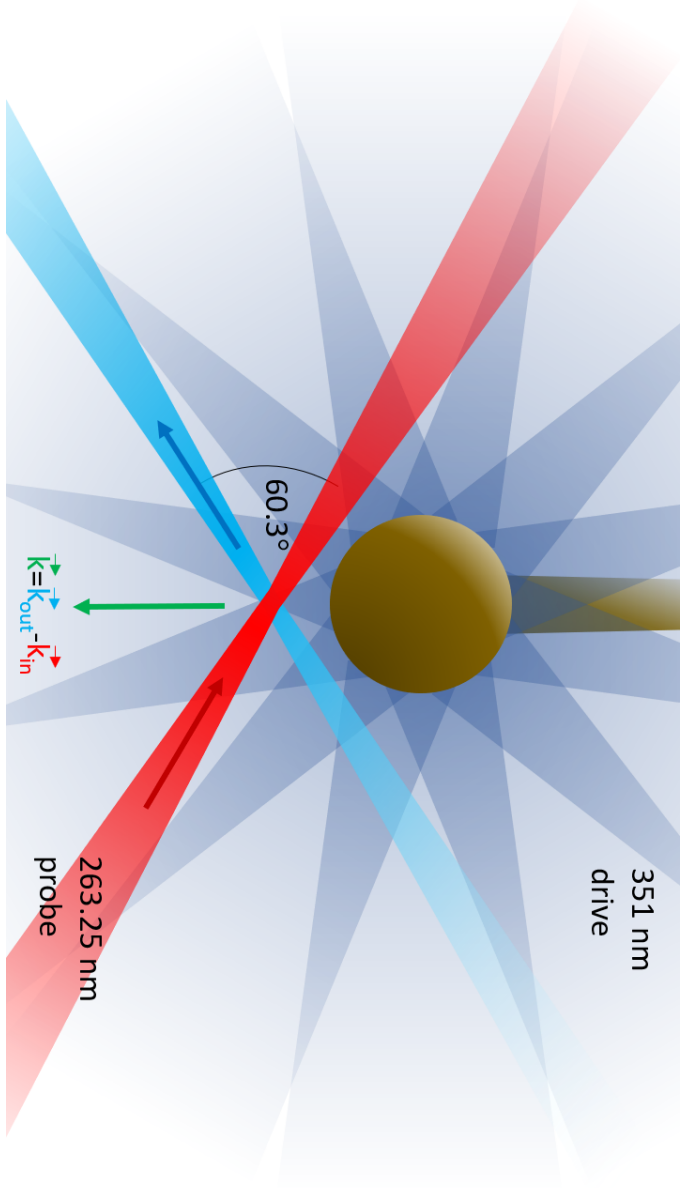

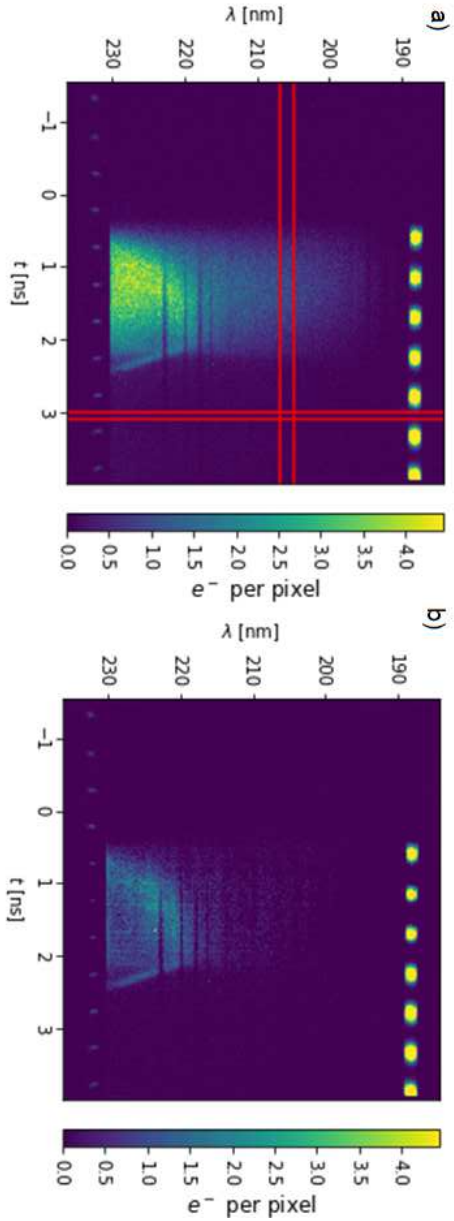

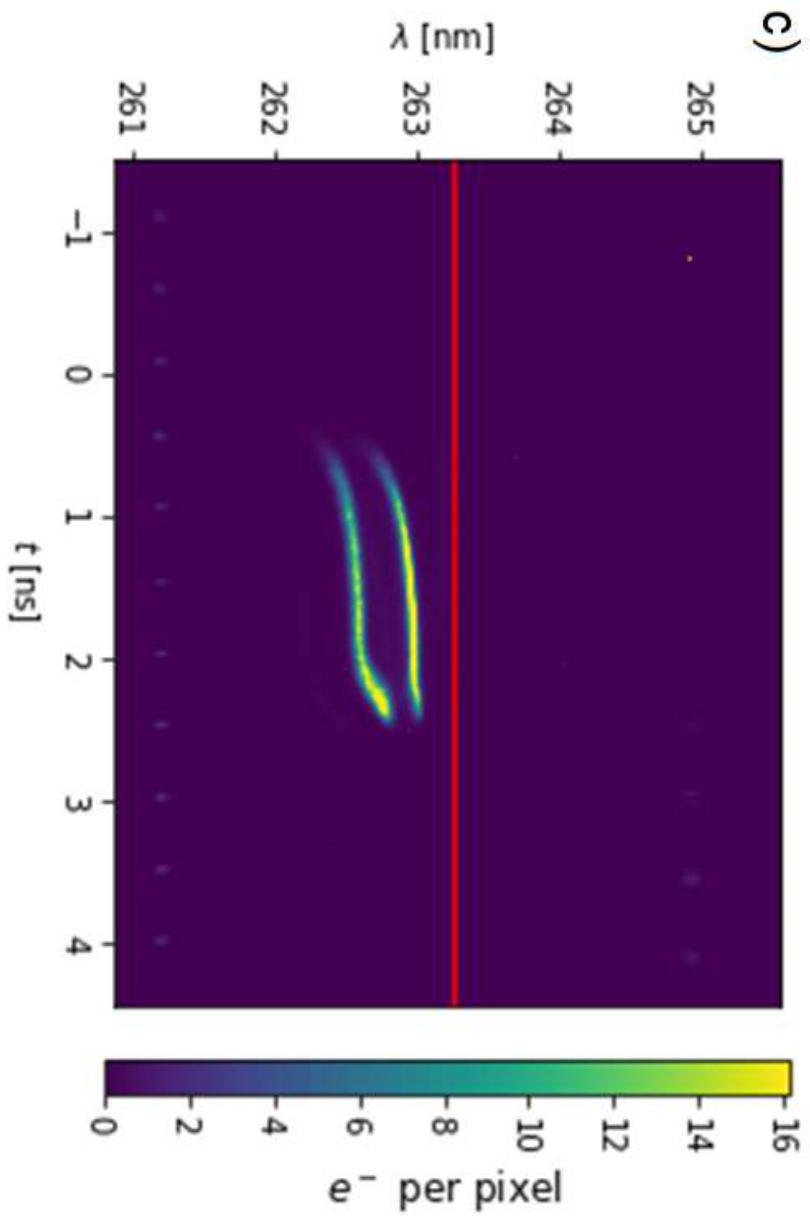

PLEASE CITE THIS ARTICLE AS DOI: 10.1063/5.0060005

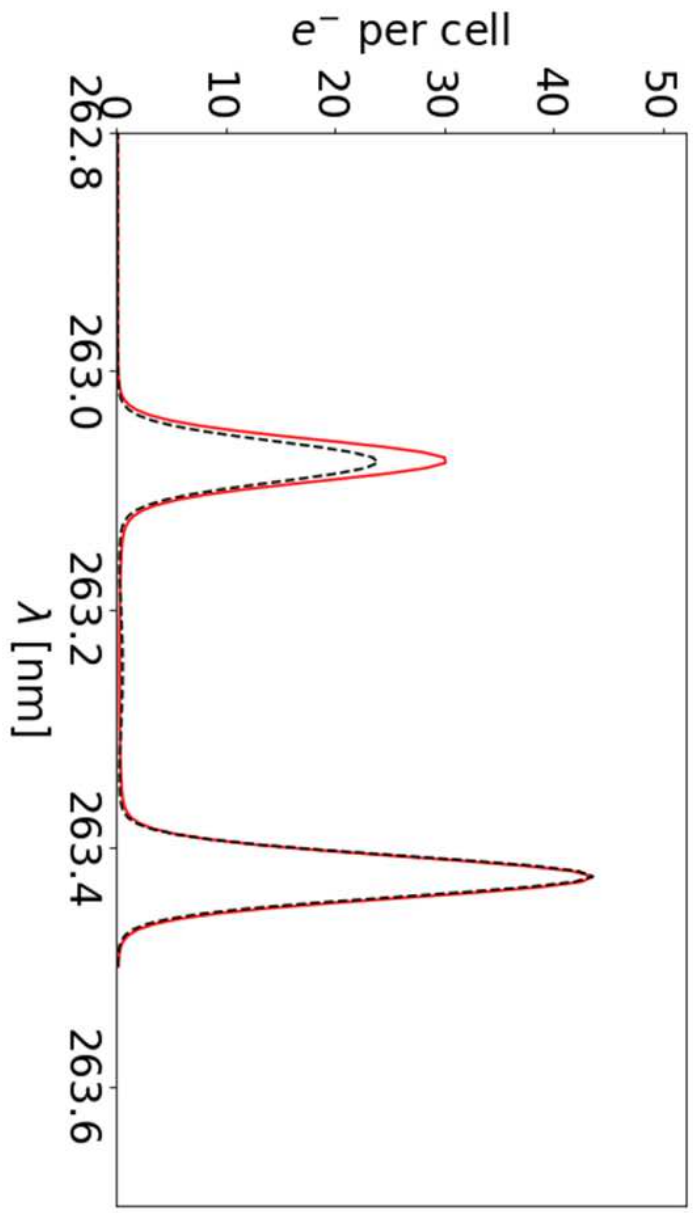

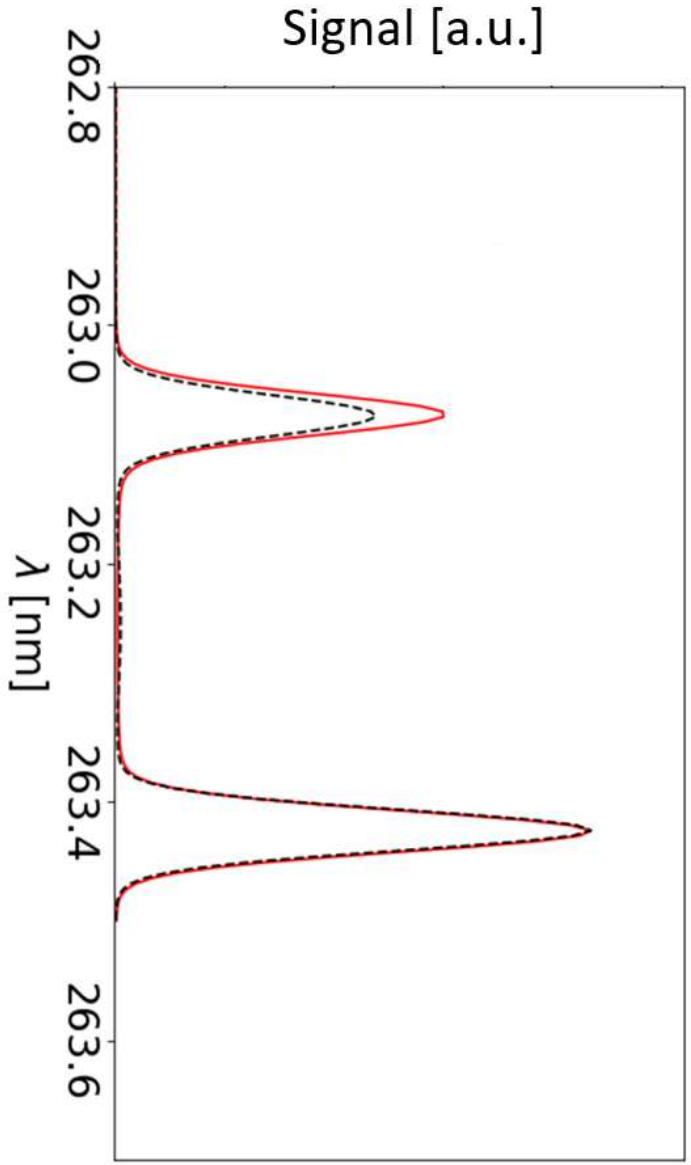

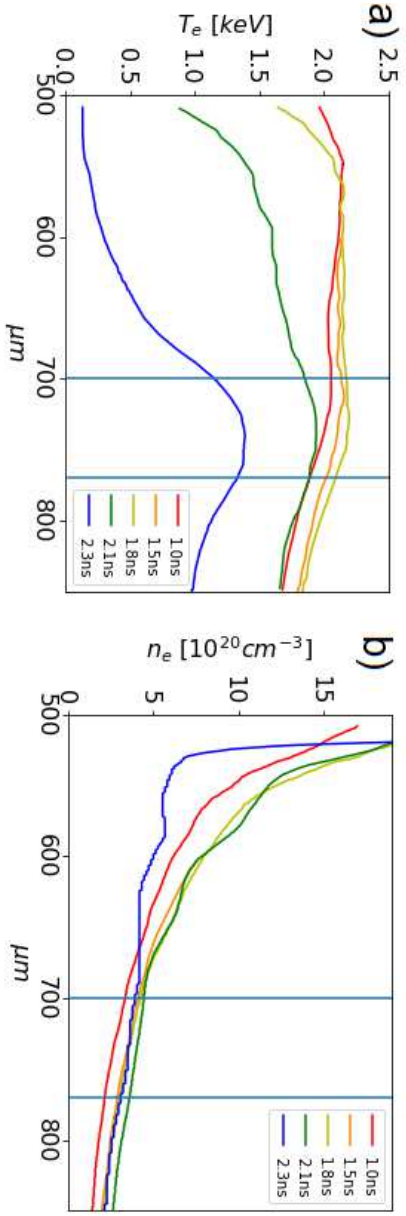

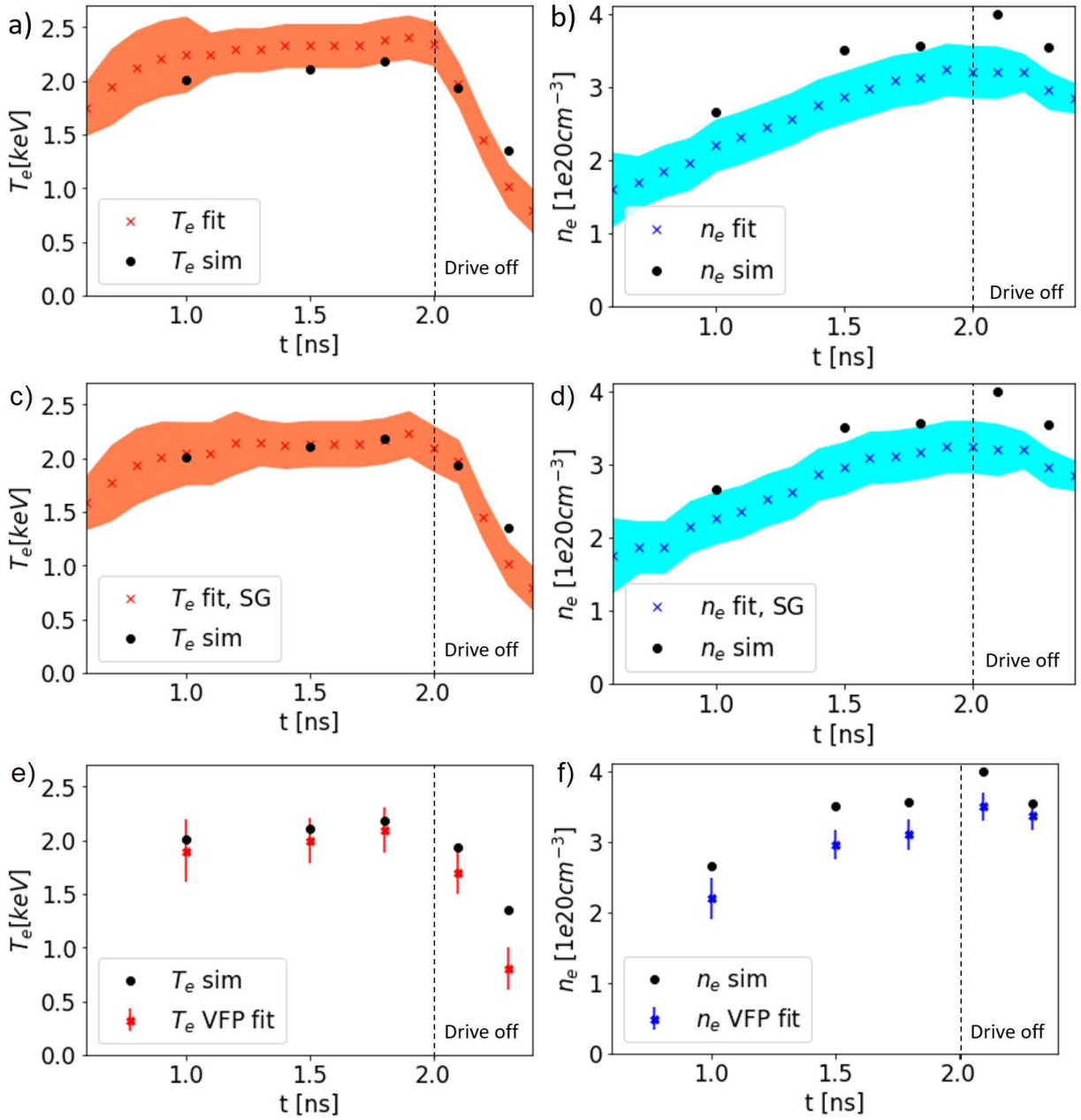

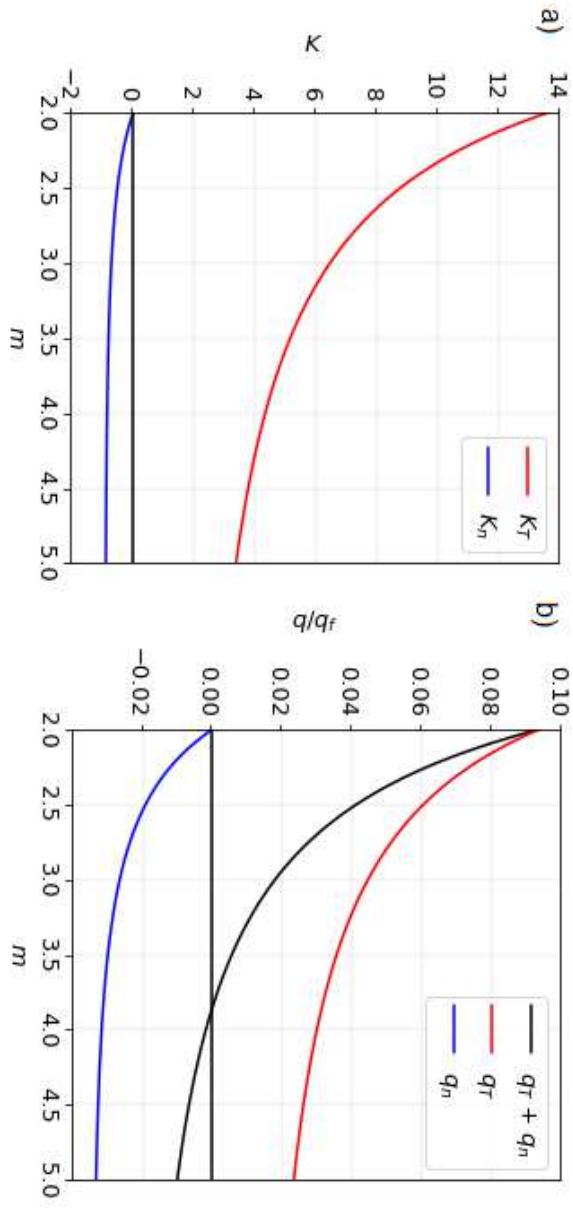

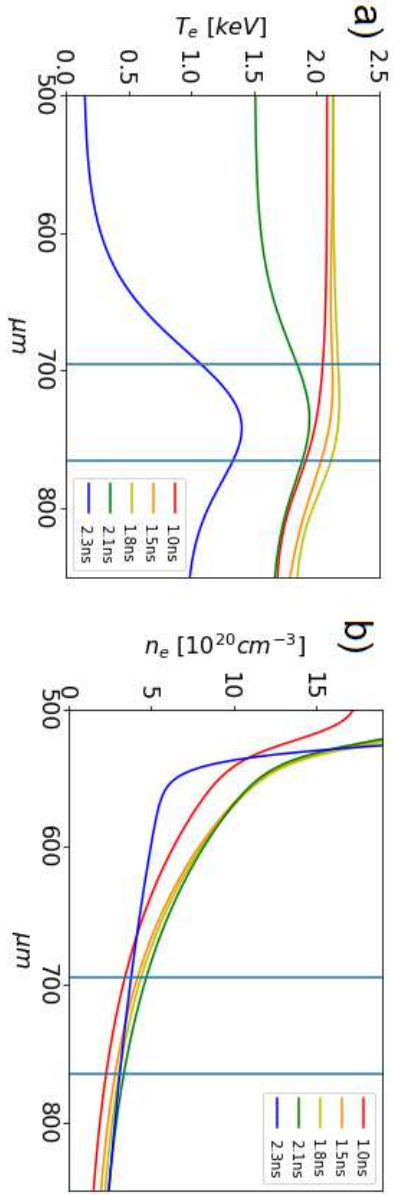

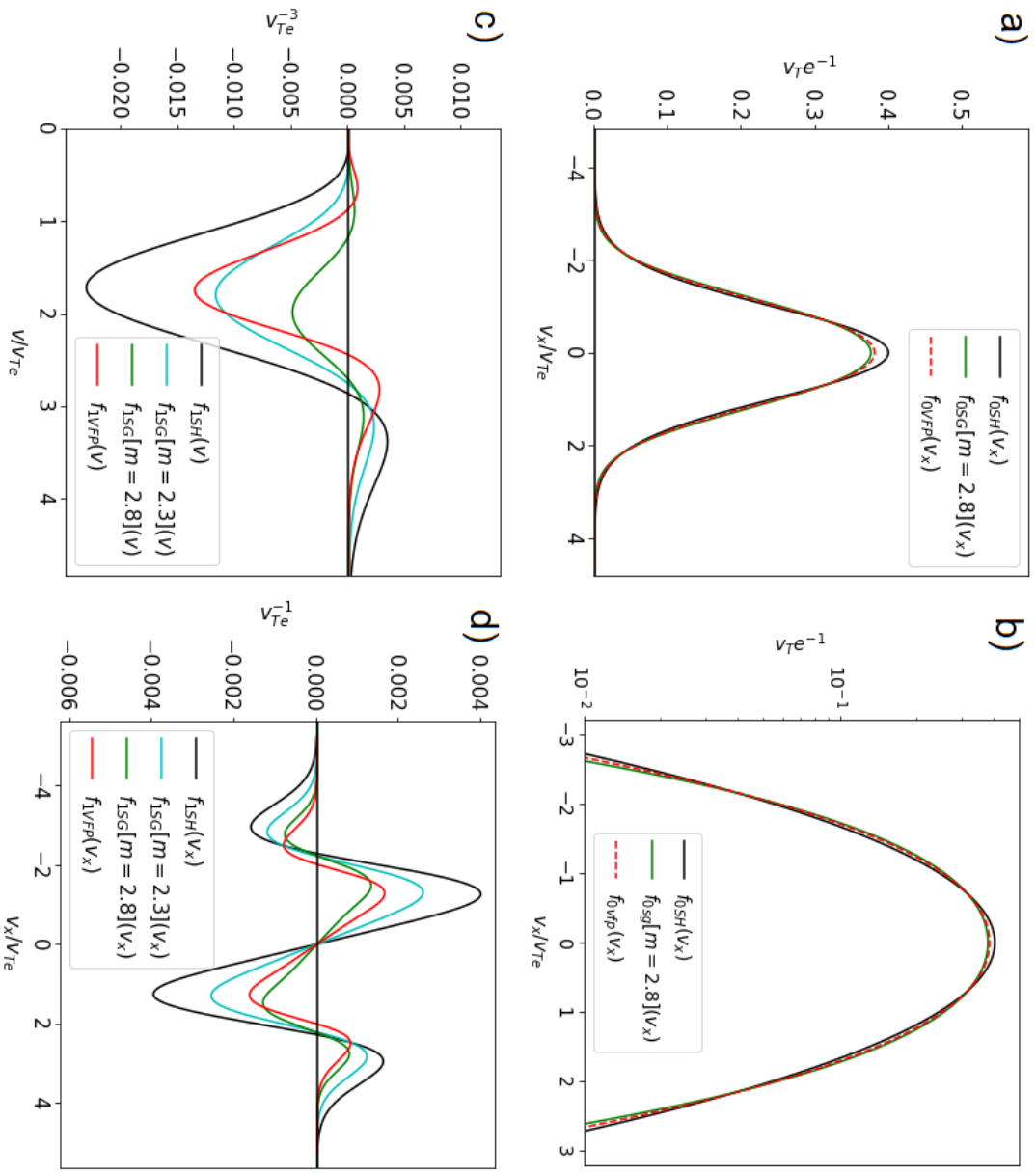

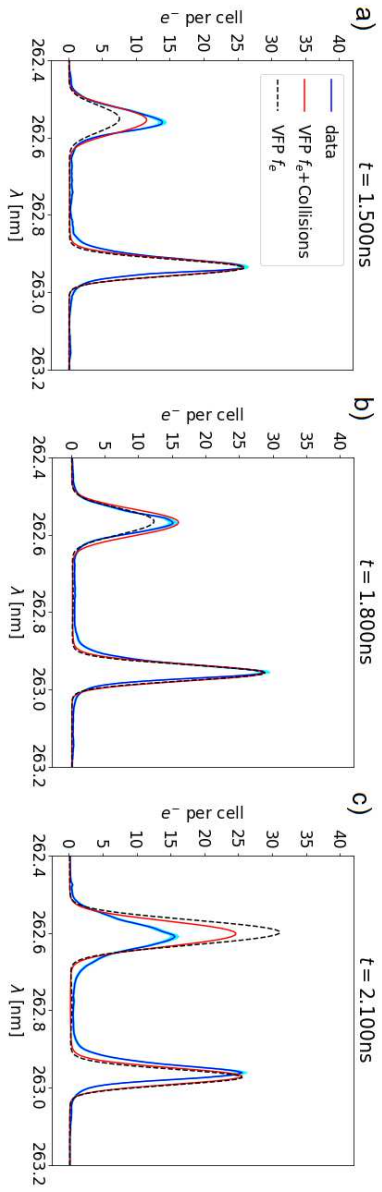

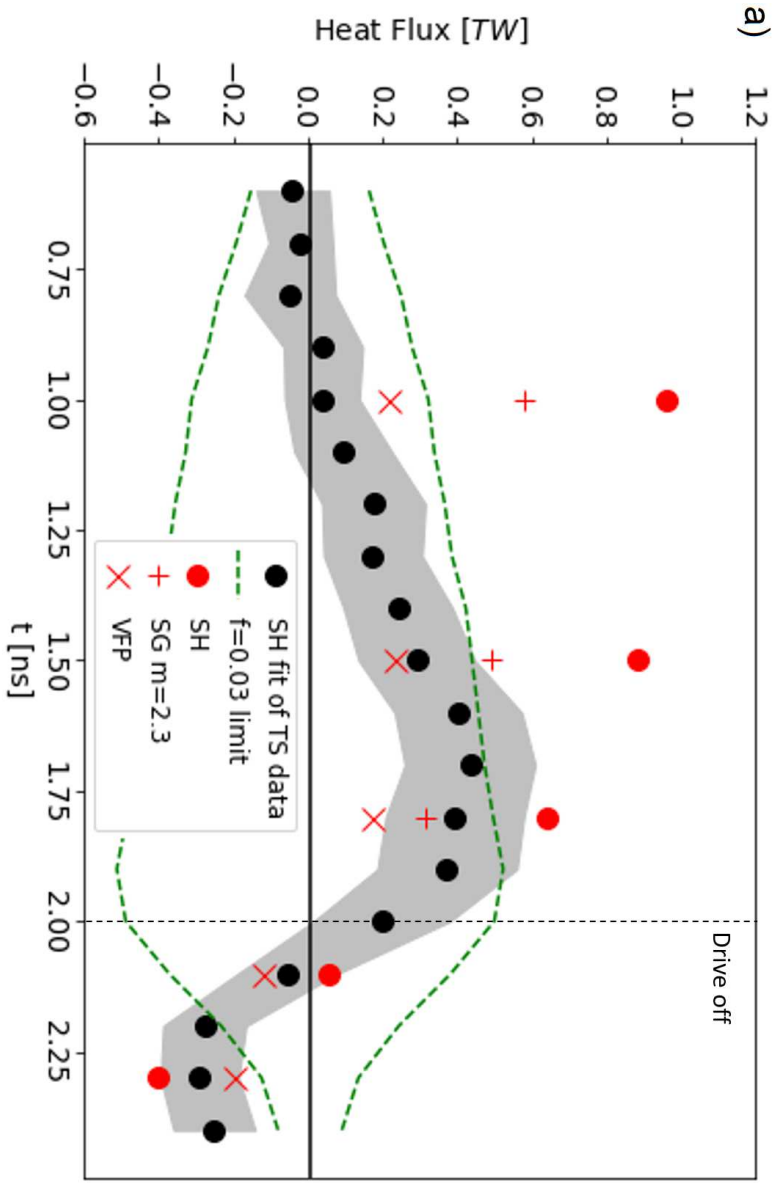

PLEASE CITE THIS ARTICLE AS DOI: 10.1063/5.0060005